



# Li distribution in graphite anodes: A Kelvin Probe Force Microscopy approach



Sergey Yu. Luchkin<sup>a,\*</sup>, Hugues-Yanis Amanieu<sup>b</sup>, Daniele Rosato<sup>b</sup>, Andrei L. Kholkin<sup>a,c</sup>

<sup>a</sup> Dept. of Materials and Ceramic Engineering & CICECO, University of Aveiro, 3810-193 Aveiro, Portugal

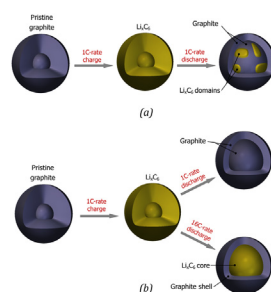
<sup>b</sup> Advanced Functional and Sintered Materials-Material Characterization and Component Design (CR/ARM1), Robert Bosch GmbH, Postfach 10 60 50, 70049 Stuttgart, Germany

<sup>c</sup> Ural Federal University, Lenin Ave. 51, Ekaterinburg 620083, Russia

## HIGHLIGHTS

- We observed a core–shell surface potential on graphite particles of an aged anode.
- We observed a mosaic surface potential on graphite particles of an unaged anode.
- Our results corroborate “radial” and “mosaic” models of Li distribution.

## GRAPHICAL ABSTRACT



## ARTICLE INFO

### Article history:

Received 30 April 2014

Received in revised form

17 June 2014

Accepted 25 June 2014

Available online 7 July 2014

### Keywords:

Li battery

Anode

Graphite

C rate

KPFM

## ABSTRACT

Advanced Li-ion batteries with high energy and power densities are urgently required in many applications including automobiles. Aging of these batteries and irreversible capacity loss are still the factors preventing their further use, and novel methods of their study are prerequisite for the understanding of degradation at nanoscale. In this work, we use Kelvin Probe Force Microscopy (KPFM) to assess the distribution of surface potential in graphite anodes of commercial Li-batteries before and after aging at high C rates. In the aged sample, we observed an apparent core-shell-type potential distribution on large crack-free particles. We attribute this core-shell potential distribution to the remnant  $\text{Li}^+$  ions stacked in graphite particles causing irreversible capacity loss. The results corroborate the “radial” model used to explain the specific capacity fading mechanism at high C rate cycling in commercial batteries.

© 2014 Elsevier B.V. All rights reserved.

## 1. Introduction

Growth in popularity of electric vehicles and green technologies requires safe, long lasting, and high performance batteries. Conventional Li-ion batteries are only efficient for low-current applications such as mobile devices, but do not satisfy the needs of

emerging high-power automotive and renewable energy applications. Higher cycling rate (C rate) in these devices causes faster degradation and lower specific capacity after prolonged use [1]. The improvement and optimization of Li-ion batteries require a complex study of the implemented electrode materials (cathode, anode and electrolyte) all involved in Li transfer. It is prerequisite to study the Li transport and diffusion at the highest resolution possible for deeper understanding of the aging processes taking place in battery materials during intensive cycling.

\* Corresponding author.

E-mail addresses: [luchkin@ua.pt](mailto:luchkin@ua.pt), [useluch@gmail.com](mailto:useluch@gmail.com) (S.Yu. Luchkin).

Scanning Probe Microscopy (SPM) based techniques such as Electrochemical Strain Microscopy (ESM) [2] and Kelvin Probe Force Microscopy (KPFM) [3] were therefore used to study aging mechanisms at the meso- and nanoscales (i.e. within the grains of active materials). Recently, Nagpure et al. have implemented KPFM to measure the surface potential (SP) of aged and unaged  $\text{LiFePO}_4$  cathodes [4]. They found that the surface potential of aged samples is lower than of the unaged ones. In another work, Jing Zhu et al. [5] used KPFM to study the change of surface potential of the  $\text{TiO}_2$  anode in an all-solid-state Li-ion battery during Li insertion and extraction. These works clearly demonstrated a great potential of KPFM for the characterization of battery materials at the mesoscale. However, stronger experimental evidence is required in order to implement KPFM quantitatively with respect to Li concentration in host material.

In this work, we used KPFM to study aging phenomena of the commercial 18650 Li-ion batteries with a graphite anode and a typical capacity of 1200 mAh. We measured surface potential in fresh and aged [ $<80\%$  State of Health (SOH), discharged at 16C-rate] graphite anodes: one from a discharged cell and the other one from a half charged cell. We observed a clear core–shell surface potential distribution within big dense particles of the aged sample in contrast to the fresh sample. Such structure is attested to remnant  $\text{Li}^+$  ions stacked in the core region of the particles. The obtained results are used to explain the specific capacity fading at high C rates caused by degradation within the active grains.

## 2. Methodology

First, a Li-ion battery cell (“fresh” further in the text) was completely discharged at 1C-rate in CC/CV mode down to 2.3 V with a stop current of 0.2C-rate. A second Li-ion battery cell (termed “aged” further in the text) was cycled being charged at 2 A (slightly more than 1C-rate) and discharged at 16C-rate (Fig. 1). After aging down to 80% SOH, it was finally discharged at 1C-rate. A third Li-ion battery cell (called “lithiated” further in the text) was cycled as the second one down to 78% SOH, then cycled two times at 1C-rate, and charged to 50% State of Charge (SOC) at 1C-rate.

The batteries were opened in an argon filled glovebox; graphite anodes were extracted, carefully washed in dimethyl carbonate (DMC), and embedded in a soft and compliant epoxy resin. After hardening the samples were sequentially polished with 1200–4000 silicon carbide sand paper, 3  $\mu\text{m}$  and 1  $\mu\text{m}$  diamond

paste, and Struers OP-S suspension. Final ion polishing was made by an Ar ion beam: 15 min cleaning at a  $10^\circ$  angle and 30 min polishing at a  $4^\circ$  angle. RMS roughness measured on cross-sections of graphite particles was  $11.1 \pm 0.4$  nm.

Surface potential of the samples was measured by means of a 2-pass amplitude modulated Kelvin Probe Force Microscopy (AM-KPFM) [6] implemented in the NT-MDT Solver Next commercial SPM. In this technique, surface potential is generally a measure of the work function difference between the tip and the sample:

$$V_{\text{CPD}} = \frac{W_{\text{tip}} - W_{\text{sample}}}{e} \quad (1)$$

Here  $W_{\text{tip}}$  is the work function of the SPM tip,  $W_{\text{sample}}$  is the work function of the sample,  $e$  is the elementary charge,  $V_{\text{CPD}}$  is the measured contact potential difference, viz. surface potential. During the first pass, the cantilever measures the surface topography, during the second pass the lifted cantilever follows the surface topography at a given height and measures the surface potential via a null method. AC voltage of the second pass was 0.5 V in amplitude, lifting height was always 15 nm; scan resolution is  $256 \times 256$  points.

It is known that AM-KPFM has lower special resolution than FM-KPFM [7,8]. However, AM-KPFM has higher sensitivity to contact potential difference (energy resolution) and can detect lower minimum detectable  $\Delta V_{\text{CPD}}$  as compared to FM-KPFM [6,8]. Higher sensitivity is important for the detection of smallest changes in surface potential caused by gradual change of Li concentration in graphite. To avoid the shift of SP measured on a biased device in AM-KPFM mode, [7] the investigated samples were not biased.

We used Pt/Ir coated cantilever (NTMDT NSG10, resonance frequency = 249.4 kHz, force constant =  $11.8 \text{ N m}^{-1}$ ) that was calibrated on sputtered Au thin film. Calibration and measurements were performed in ambient conditions at relative humidity (RH) 40%. Measured contact potential difference between the Au film and the tip was  $V_{\text{CPD}} = (57.8 \pm 0.3) \text{ mV}$ . According to the recommended values of work functions [9] (see Table 1),  $V_{\text{CPD}}$  should be in the  $-(19\text{--}11) \text{ mV}$  range. The difference can be explained by the impact of the ambient humidity, resulting in the absorbed water layer that can screen the work function difference. [10] Note that presented in literature work function values for Au and Pt are scattered in a wider range as compared to those presented in Table 1.

## 3. Results and discussion

The cycle life of the aged cell shows a clear activation step during the 5 first cycles, i.e. the discharge capacity increases (see Fig. 2). The 20 following cycles show a slow decrease in the capacity. This behavior can be explained by the fact that some lithium ions are not yet activated. Two processes with opposite trends run in parallel. On one hand, more and more lithium ions are involved into an electrochemical process upon cycling, increasing the capacity. On other hand, some lithium ions are being consumed due to ageing phenomena, hence being passivated and decreasing the capacity. After a while the first process becomes insignificant, explaining the

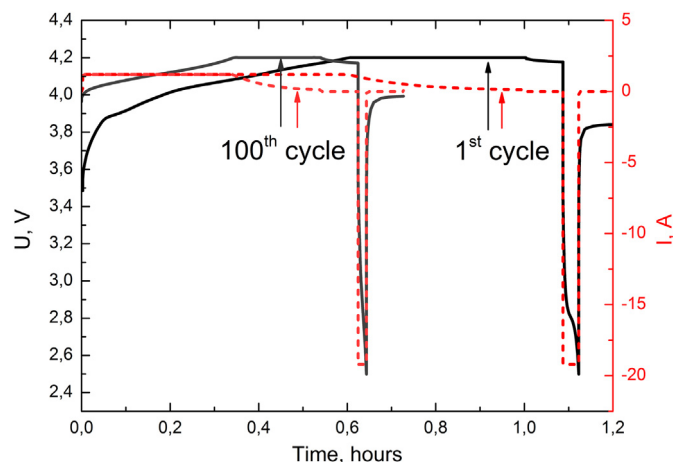
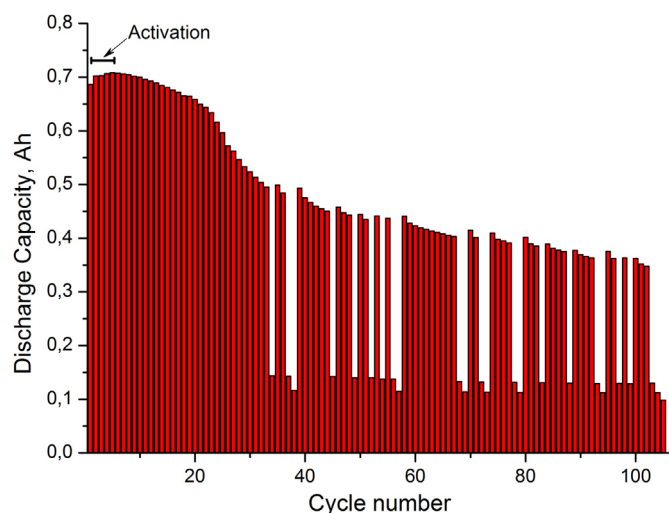


Fig. 1. Charge-discharge curves of the aged to 80% SOH sample for the 1st and the 100th cycles. Battery was charged in the CC/CV mode at 2 A current until voltage reach 4.2 V and then discharged at 16C-rate.

Table 1  
Recommended work functions for polycrystalline materials [9].

Material (polycrystalline)	Work function, eV
Au	$5.31 \pm 0.07$
Pt	$5.27 \pm 0.08$
Cu	$4.51 \pm 0.07$
Graphite	$4.6 \pm 0.1; 5.0$



**Fig. 2.** Discharge capacity versus cycle number of the aged cell. The 5 first cycles present a capacity increase due to activation of the cell. The very low capacities are due to failure with the cycling instrument (courtesy of ZSW).

transition in the cycle life. Owing to the fact that we did not observe the incipient capacity drop, we assume that the initial Solid Electrolyte Interface (SEI) formation was already done by the cell manufacturer.

With increasing number of cycles the capacity drops suddenly ( $>25$  cycle). This might be due to other processes consuming lithium ions (e.g. the initial SEI cracking and new SEI formation during fast discharge, SEI thickening, etc.) [11,12] and hence drastically decreasing the performance of the cell. Note that the cycles with very low capacity are due to sudden high internal resistances while discharging, bringing the voltage to the set minimum voltage threshold.

Fig. 3 (a, b) illustrates simultaneous mapping of the topography and surface potential of the fresh anode. Graphite particles and a Cu current collector are clearly distinguishable inside a polyvinylidene fluoride (PVDF) binder filled with the epoxy resin. Surface potential on the graphite particles is not uniform: there are internal regions with reduced down to 200 mV surface potential (Fig. 3 (b), dark color). Cross-section of KPFM signal (Fig. 3 (b) – line 1, Fig. 3 (c))

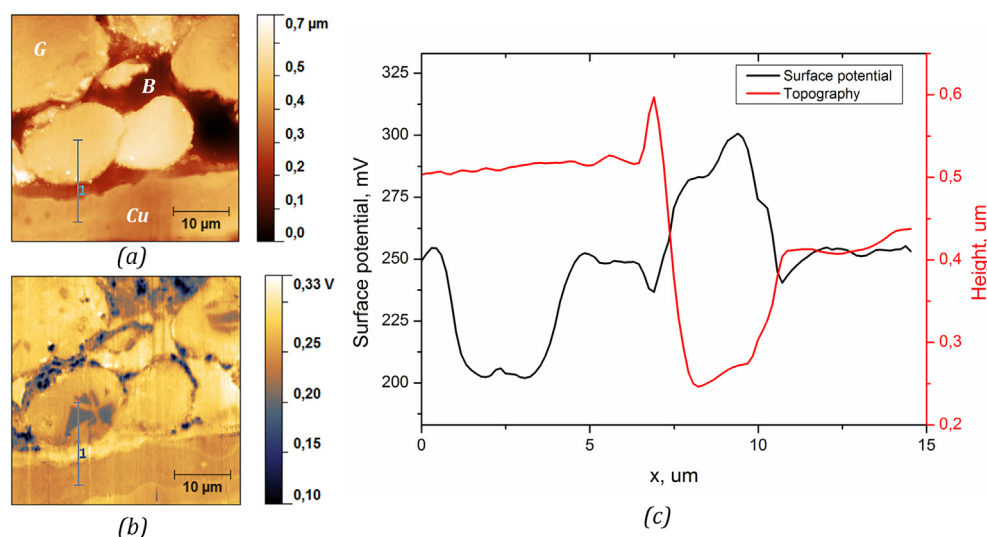
clearly demonstrates that surface potential within these regions is plane around 200 mV with sharp boundaries.

Though the surface potential image looks similar to the topography image, it is not due to the topography crosstalk. The sample is a composite that contains a number of different materials, viz. copper, graphite, PVDF with carbon black, and epoxy. Each of these materials has its own surface potential, therefore the topography and the surface potential images correlate with each other but not identical. The comparison of the surface potential profile with the topography profile (Fig. 3 (c)) unambiguously proves that the reduced potential does not come from the topography crosstalk.

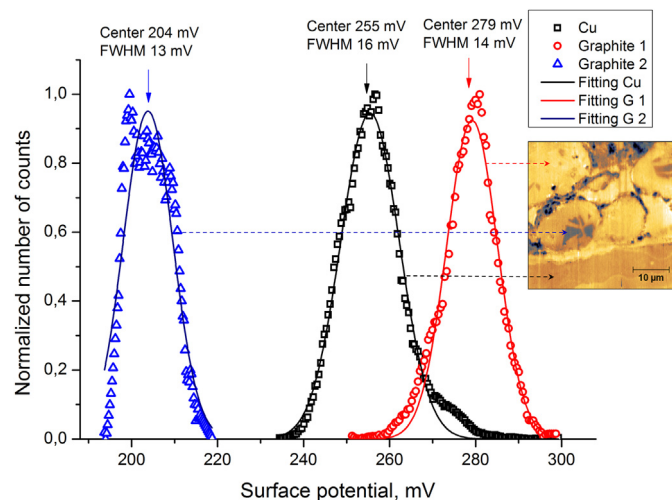
The surface potential distribution obtained from the scan presented in Fig. 3 (b) contains several peaks assigned to the Cu current collector, the “normal” graphite, and the graphite with the reduced potential (internal spots). These peaks are presented in Fig. 4. All peaks are narrow enough with a similar full width at half maximum (FWHM) and without broad transition regions (as for the aged sample, see below). It indicates uniform composition of the areas from which the peaks were collected.

Fig. 5 (a, b) illustrates the topography and surface potential of the aged sample. Surface potential of the graphite particles strongly depends on the particle mechanical integrity. Several particles on the upper half of the topography image have open cracks that are filled with epoxy (that also prove cracks are not due to the polishing process). Surface potential on these graphite particles is less uniform and is lower (Fig. 6, “Graphite 1” peak) than in the fresh sample, but not as low as on the dense particles on the bottom half of the image. Surface potential on the big ( $\approx 25 \times 15 \mu\text{m}$ ) dense particle forms the core–shell structure with almost linear decay of the surface potential in the  $\approx 5 \mu\text{m}$  shell region toward the constant bottom level in the core region (Fig. 5 (b, c)). The shell region corresponds to the broad transition part in the surface potential peak in Fig. 6 (“Graphite 2” peak). The reduced potential in the core corresponds to the narrow peak at the end of the transition region in Fig. 6. Small ( $\approx 10 \mu\text{m}$ ) dense particle in contact with the big one shows quite low SP without the core–shell structure.

Peak distribution in Fig. 6 clearly demonstrates that the Cu surface potential peak remains narrow without transition regions – similar to the Cu surface potential peak of the fresh specimen. On the contrary, both graphite peaks are drastically different in comparison with the fresh sample: they are much broader and have transition regions.



**Fig. 3.** Topography (a), surface potential (b), and cross-sections (c) of the fresh graphite anode. On the topography image “Cu” denotes the Cu current collector, “G” – active graphite particles, “B” – carbon black enriched with PVDF binder filled with epoxy. Notice regions of the reduced surface potential inside graphite particles on the surface potential image (b).



**Fig. 4.** Surface potential distribution from Cu and graphite parts of the fresh sample. Arrows show corresponding surface potential on the surface potential image of the sample.

A total of  $8000 \mu\text{m}^2$  were scanned in order to exclude the statistical error. Each crack-free particle with more than  $10 \mu\text{m}$  minimum size has similar core-shell type of surface-potential with the shell width around  $5 \mu\text{m}$ .

For  $40 \times 40 \mu\text{m}$  scan size with  $256 \times 256$  points density the resolution is  $156 \text{ nm point}^{-1}$ . Taking into account  $10\text{--}50 \text{ nm}$  thickness of SEI layer [13] and blur effect of the absorbed water layer the resolution is not sufficient to observe the SEI layer effect on edges of graphite particles.

### 3.1. Impact of humidity

The measurements were done under ambient conditions, there is therefore an inevitable absorbed water layer on top of the surface. It is well known that the absorbed water layer screens surface potential due to the formation of dipoles. Hence, the measured potential difference is lower than the actual one. Different authors have reported different impacts of absorbed water. Bluhm et al.

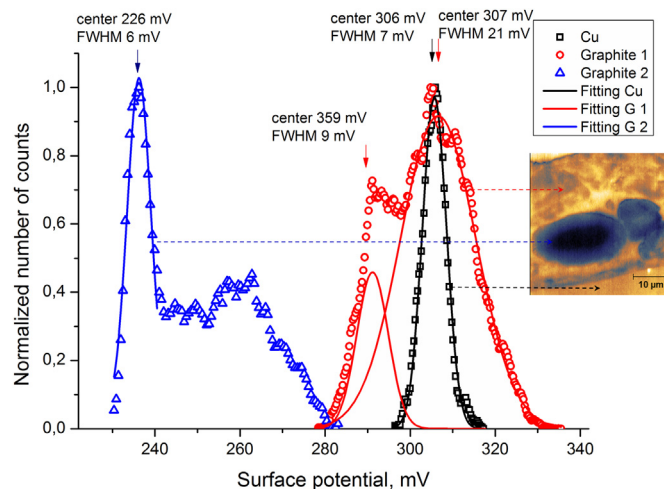


**Fig. 6.** Surface potential distribution from Cu and graphite parts of the aged sample. Arrows show corresponding surface potential on the surface potential image of the sample.

[10] demonstrated a decrease of the surface potential on the dry mica from  $+350 \text{ mV}$  at  $\text{RH} = 0\%$  down to zero at  $\text{RH} = 40\%$ . Zaghloul et al. [14] documented similar results on  $\text{SiN}_x$  surface, where surface potential of the trapped charge is reduced from  $\approx 5 \text{ V}$  at  $\text{RH} = 0.02\%$  to  $\approx 2 \text{ V}$  at  $\text{RH} = 40\%$ . On the other hand, Hansen and Hansen [15] reported almost negligible contribution of humidity to the measured surface potential in highly ordered pyrolytic graphite (HOPG). Ono et al. [16] found that the surface potential of InAs decreased more than 25% after the thermal treatment that removed the absorbed water layer from the surface. Obviously, the humidity impact on the KPFM results strongly depends on the type of probed material due to its different hydrophobicity.

We consider the impact of humidity only on the graphite and Cu surfaces and ignore the epoxy. Based on the calibration data taken on the gold thin film (see the Methodology section), we assume that the impact of the absorbed water layer on the graphite and Cu potential is similar and  $\sim 50 \text{ mV}$ .

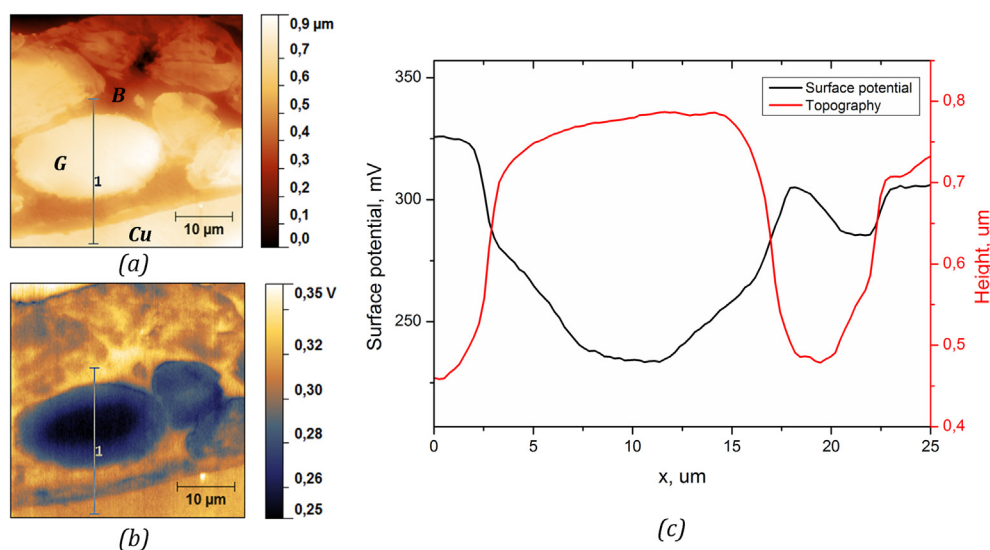


**Fig. 5.** Topography (a), surface potential (b), and cross-sections (c) of the aged graphite anode. On the topography image “Cu” denotes the Cu current collector, “G” – active graphite particles, “B” – carbon black enriched with PVDF binder filled with epoxy. Core-shell structure is evident on the big dense particle on the surface potential image (b).



### 3.2. Effect of the Cu oxide layer

Another reason of surface potential deviation from the table values of the work function difference (see Table 1) is presence of oxides. We consider only the Cu current collector surface because it did not degrade during cycling and can be used as a reference, so, apart of the absorbed water, only  $\text{Cu}_2\text{O}$  can change the surface potential. According to Przychowski et al., [17] the presence of copper oxide leads to significant increase of the work function as compared to the pure metal. They reported a change in the work function from 4.45–4.95 eV on the pristine surface to 4.65–5.05 eV on the surface exposed to oxygen. Remarkably, the work function increased with time of exposition and tended to reach saturation at 5.05 eV. According to Equation (1), it is equal to drop of the surface potential on the oxidized surface as compared to the unoxidized one. Using data from Table 1, the work function difference between Pt and Cu is  $W_{\text{Pt}} - W_{\text{Cu}} = (0.76 \pm 0.11)$  eV. Using data from Przychowski et al., [17]  $W_{\text{Pt}} - W_{\text{Cu/Cu}_2\text{O}} \approx 5.3 - 5.05 = 0.25$  eV that is equal to 0.25 V surface potential value. Hence, the copper oxide should decrease the measured surface potential down to 250 mV. The copper surface potential peaks in Figs. 4 and 6 are in the same range  $\approx (250\text{--}300)$  mV (i.e., 0.25–0.30 eV) being in a good agreement with the above result.

Further we use the Cu surface potential as a reference value that should be the same for both samples and which shift is related to the RH change. Quantitative comparison of the graphite surface potentials from different samples is done with respect to the Cu surface potential.

### 3.3. Graphite surface potential

Fig. 4 reveals that the surface potential value of graphite on the fresh sample is  $279 \pm 14$  mV. According to Table 1,  $W_{\text{Pt}} - W_{\text{G}} \approx 5.3 - (4.5\text{--}5.0) = 0.6\text{--}0.3$  eV (i.e., equal to 600–300 mV). Therefore, the experimental value of the graphite potential is in a good agreement with the table data if the graphite work function  $\approx 5.0$  eV. Small difference can be attributed to the absorbed water layer.

### 3.4. Surface potential reduction

We suggest three possible physical mechanisms of the observed surface potential change in graphite anode: graphite structural disorder, Li intercalation, and appearance of reaction products and following contamination of the surface.

Structural disorder of graphite during cycling is a well known phenomenon. Obraztsov et al. [18] have shown that disordered graphite with  $\text{sp}^3$ -like defects in  $\text{sp}^2$  network possesses a lower work function as compared with highly ordered pyrolytic graphite (HOPG). According to Equation (1), this should apparently result in the surface potential increase. However, experimental results show that graphite of fresh and aged anodes has surface potential equivalent to the fresh graphite work function (Fig. 3 (b)) or lower (Fig. 5 (b)), i.e. opposite to what is expected. This rules out the structural disorder effect as a main contribution to the surface potential variation.

Another possible source of the surface potential change is the existence of remnant  $\text{Li}^+$  ions in the graphite active particles. It is long time known that the doping of graphite with alkali, alkali-earth, and rare-earth elements leads to the formation of a surface dipole layer that reduces the initial work function. [19] Thus, Li-intercalated graphite must have lower work function as compared with the fresh graphite. According to Equation (1), it should also result in higher surface potential that is not the case. It

means that Li intercalation may not be a dominant mechanism responsible for the observed effect.

As pointed out above, the KPFM measurements were done under ambient conditions, i.e. the anode samples (polished cross-sections) were exposed to humid atmosphere. The lithiated graphite is not stable in ambient conditions, hence we suggest that  $\text{Li}^+$  ions react with the ambient gases and absorbed water and form a layer of reaction products on the graphite surface. The surface film typically is a mixture of the following reaction products:  $\text{Li}_2\text{O}$ ,  $\text{Li}_3\text{N}$ ,  $\text{LiOH}$ , and  $\text{Li}_2\text{CO}_3$ . All these compounds reduce the overall surface potential relative to the fresh graphite. [20–22] Moreover, the thicker layer of the products – the stronger should be the surface potential reduction. [20] Hence, the observed decrease of the surface potential on the cross-sections of the graphite active particles in the aged sample can be attributed to the surface layer of the Li reaction products. We believe that almost linear decline in the shell region is a natural result of the increasing thickness of the surface film towards the core region that correlates with the Li concentration in the graphite material underneath. Consequently, the lowest surface potential in the core region must correspond to the highest Li concentration in the graphite anode.

To confirm the proposed model we studied the lithiated sample with 50% SOC. At this SOC significant concentration of Li is certainly present in the graphite anode. Under ambient conditions the layer of reaction products is formed on the surface. Measured surface potential and topography are shown in Fig. 7. The topography after the ion polishing is equivalent to the fresh and the aged samples without specific features such as metallic Li particles. The surface potential of the graphite particles is suppressed as compared to graphite of the fresh sample without  $\text{Li}^+$  ions (Fig. 3). Note, that in the proposed model higher Li concentration (and the thicker reaction products surface layer) results in the lower surface potential. Using the Cu surface potential ( $V_{\text{Cu}}$ ) as a reference, for the suppressed surface potential regions of graphite  $V_{\text{Cu}} - V_{\text{G}} \approx 75$  mV for the fresh sample,  $\approx 81$  mV for the aged sample, and  $\approx 135$  mV for the lithiated 50% SOC sample. This clearly supports the proposed model of the surface potential suppression.

Note that the effect of the surface film should disappear when anode is not exposed to humid atmosphere and the KPFM measurements are done under controlled inert atmosphere.

### 3.5. Explanation of the shape of reduced surface potential regions

For quantitative estimation, we take the Li diffusion coefficient in graphite in the range  $10^{-9}\text{--}10^{-10}$   $\text{cm}^2 \text{ s}^{-1}$ . [23] Based on these values and using Equation (2), the expected Li diffusion length at 1C-rate is (6–20)  $\mu\text{m}$  and at 16C-rate is (1.5–5.0)  $\mu\text{m}$ . Thus, at 1C-rate Li can completely deintercalate from a particle with up to 40  $\mu\text{m}$  size, while at 16C-rate Li can deintercalate from a particle with up to 10  $\mu\text{m}$  size as predicted by a simple formula:

$$l = \sqrt{D\tau}. \quad (2)$$

Here  $D$  is the Li diffusion coefficient,  $\tau$  is the diffusion time,  $l$  is the diffusion length.

Concerning the fresh cell, the discharged was made at a lower C rate. The lithium ions had enough time to deintercalate from the particles. During lithiation/delithiation graphite passes through a staging phenomenon where at least two phases coexist within a single graphite grain [24]. Direct observation of coexistence of two phases was made by Funabiki et al. [25] They observed the stage 4 within the dilute stage 1 (explained elsewhere) with a sharp phase boundary. The stage 4 propagated either from the edge plane or from defects (cracks) in the basal plane. The phase boundary movement was significantly retarded by cracks.

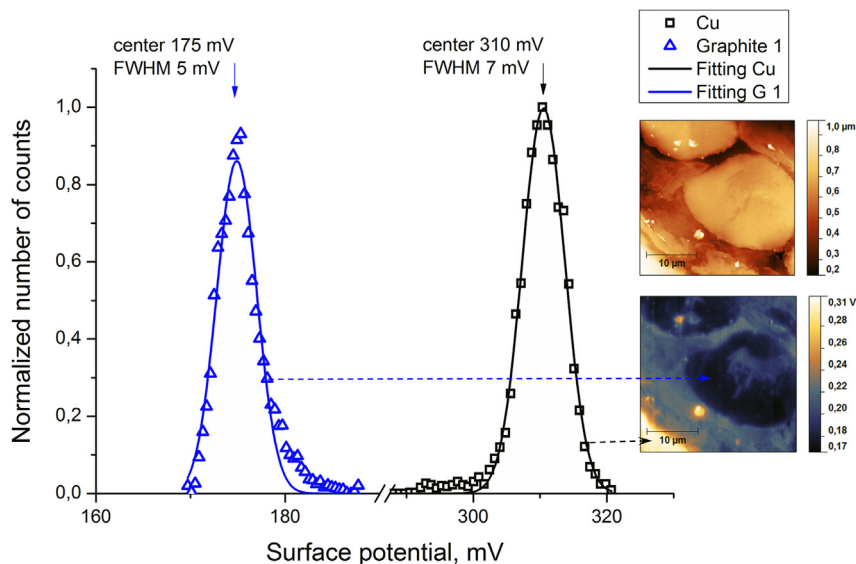


**Fig. 7.** Surface potential distribution from Cu and graphite parts of the lithiated sample. Arrows show corresponding surface potential on the sample. Right top and bottom images are topography and surface potential respectively.

In this sample (Fig. 3), the observed regions of reduced surface potential with sharp boundaries might be domains of remaining  $\text{Li}_x\text{C}_6$  within delithiated graphite. Though we did not detect any cracks, we can think of dislocation walls that antedate cracking. If the graphite particle is an agglomeration of several grains then pinning is possible at the grain boundaries. As explained at the beginning of Section 3, there is an activation step in the cycle life due to lithium ions which are not yet actively participating in the electrochemical process. These regions could explain the following phenomenon: during the first cycles, lithium ions are trapped in the inner layer where the staging phenomenon is stopped. Upon cycling, deformation of the active material leads to activation of trapped lithium ions. One of the possible causes is movement of dislocation walls.

In the 16C-aged sample deintercalation was not complete. The output battery voltage at a constant current is a combination of a battery electrochemical potential ( $E_0$ ) and a potential determined by internal resistance ( $R_{\text{internal}}$ ): [11]

$$V = E_0 - IR_{\text{internal}}. \quad (3)$$

Internal resistance consists of several components such as electrolyte resistance, polarization, SEI layer, etc., but one important cause of increasing resistance is the loss of mobile charges, i.e.  $\text{Li}^+$  ions. At 16C-rate Li can pass up to 5  $\mu\text{m}$  that corresponds to the shell region size (Fig. 5 (b, c)) that is around 5  $\mu\text{m}$ . Consequently, during discharging at 16C-rate battery passes at least two steps. First step with sufficiently small internal resistance until  $\text{Li}^+$  diffusion pathway is shorter than the shell width (5  $\mu\text{m}$ ). During this step, the number of deintercalating  $\text{Li}^+$  ions is enough to provide required current. On the second step the amount of available mobile  $\text{Li}^+$  ions within the short pathway area is not enough to provide a required current, so the internal resistance leaps upwards. The total battery voltage (Equation (3)) decreases below the cut off voltage, so the battery indicates discharge though it is not fully discharged. This might explain the presence of Li in the core region during cycling and the observed core–shell surface potential structure.

The fact that during cycling with 16C-rate discharge Li was extracted only from the shell region and remained blocked in the core region due to the diffusion limitation directly correlates with

the specific capacity reduction during cycling at higher C rate as compared with lower C rate [1].

Nevertheless, after aging at 16C-rate the battery was finally discharged at 1C rate and  $\text{Li}^+$  ions might fully deintercalate from the particle, but it did not happen (according to the proposed model).

Obviously, the shell region – where Li is constantly inserted and extracted – should be much more structurally disordered as compared with the core region (where Li was inserted only during the first charge step). According to Gnanaraj et al. [26] Li intercalation mechanisms into graphite and disordered carbon are different. In the ordered graphite the Li intercalation/deintercalation is a staged process, while in the disordered carbon it is not. Linear decay of the shell region surface potential might indicate an absence of the staging phenomena. However, by potential step chronoamperometry method no correlation was found between the phase boundary movement and degree of crystallinity. [25] Therefore, different intercalation/deintercalation mechanisms cannot explain the obtained results.

Possible explanation is the continuous network of defects (such as dislocation walls) around the core. Lattice parameter  $c$  along  $z$ -axis is 3.359 Å for pristine graphite and 3.712 Å for  $\text{LiC}_6$ . [27] During high C rate cycling the core region interlayer distance (if  $\text{LiC}_6$  is the core phase) remained constant at 3.712 Å, while the shell region interlayer distance varied from 3.359 Å to 3.712 Å and vice versa. Moreover, according a model proposed by Yue Qi et al., [28] the Young's modulus of polycrystalline graphite is increased threefold during lithiation of pristine graphite to  $\text{LiC}_6$  with simultaneous weakening of C–C bonds within basal planes. Within their model, where phase transitions are: pristine graphite to  $\text{LiC}_{18}$ ,  $\text{LiC}_{18}$  to  $\text{LiC}_{12}$ , and  $\text{LiC}_{12}$  to  $\text{LiC}_6$ , the maximum tension occurs at the  $\text{LiC}_{12}$  to  $\text{LiC}_6$  transition – what we expect at the surface potential core–shell interphase. Such strong lattice parameter change between phases with different mechanical properties can lead to significant mechanical stress between the core and the shell that can break the C–C bonds [29] at the interphase. Prolonged cycling that periodically produces mechanical stress within a single area should lead to fatigue and massive structure damage on the surface potential core–shell interface. Due to the fact that Li intercalate inside layers in graphite and hardly can jump from one layer to another, significantly damaged edges within the bulk can hinder Li deintercalation.

Other important observation on the aged sample is that the surface potential distribution of the cracked particles and of the dense particles significantly differs. The big cracked particle shows higher surface potential than the dense one and without the core–shell type of surface potential (Fig. 5). It means that there are less remnant  $\text{Li}^+$  ions inside. Taking into account that all observed cracks are filled with the epoxy (Fig. 5 (a)), we can conclude that the electrolyte had access to all internal surfaces and Li diffusion paths were significantly shorter than in the dense particle of the same size. Consequently, remnant Li concentration and corresponding surface potential of a cracked particle do not depend on the particles size.

Note that the crack's surface consumes Li due to formation of new SEI layers as soon as crack is formed. This process is continuously occurring upon cycling.

Furthermore, the mosaic and radial models [30] can be introduced in order to explain the observed behavior. It summarizes the discussed above experimental data and proposed mechanisms.

According to the mosaic model (Fig. 8 (a)), inactive  $\text{Li}^+$  ions are trapped within the  $\text{Li}_x\text{C}_6$  domains after full discharge. The domain boundaries can be pinned by localized crystallographic defects such as dislocations. During cycling, lithium insertion and extraction gradually redistribute these localized defects along with generation of new randomly distributed defects. This process activates trapped  $\text{Li}^+$  ions during first several cycles (5 in the present case). The mosaic model is size independent.

According to the radial model (Fig. 8 (b)), at a high C rate a core of a blocked  $\text{Li}_x\text{C}_6$  phase is formed due to diffusion limitation: at a given C rate (discharge time) Li can diffuse at a certain length determined by Equation (2). After prolonged cycling at a high C rate the shell region is much more structurally disordered than the core one, and the continuous network of defects (C–C bonds disruption) around the core hinders Li of the core from deintercalation even at a low C rate discharge. This model is applicable only if the diffusion length is smaller than the particle radius, i.e. it is size dependable.

These two models can coexist within a single particle: experimental results suggest transition from the mosaic model at the beginning of cycling to the radial model after prolonged cycling.

#### 4. Conclusion

The fresh and aged graphite anodes of commercial Li batteries were investigated by means of KPFM. The study revealed the existence of remnant Li after delithiation within the bulk of both samples. We found that at 1C-rate small fractions of  $\text{Li}^+$  ions can be blocked as domains of  $\text{Li}_x\text{C}_6$  phase within the bulk pure graphite. After cycling at 16C-rate to 80% SOH and the final discharge at 1C-rate the apparent core–shell structure within the big dense graphite particles was observed. The core region might thus represent a “dead” volume within which the  $\text{Li}^+$  ions are blocked. Besides this, we found that cracked particles of the same size do not reveal any core–shell structure. The results are a direct visualization of the radial model that is used to describe the Li intercalation/deintercalation process in polycrystalline anode materials.

The implemented method can be used to observe Li distribution in the graphite anode at the nanoscale. Being calibrated on a reference sample with known Li concentration, this method can provide quantitative information about Li concentration in the host material at the mesoscale.

#### Acknowledgments

The work is supported by the European Commission within FP7 Marie Curie Initial Training Network “Nanomotion” (grant agreement no 290158). The authors gratefully acknowledge V. Gorshkov, K. N. Romanyuk and M. S. Ivanov for valuable discussions. We would like to thank Dr Thomas Waldmann from the “Zentrum für Sonnenenergie- und Wasserstoff-Forschung” in Ulm (ZSW) for helping us with fast cycling of the cells.

#### References

- [1] Tae-Hwan Park, Jae-Seong Yeo, Min-Hyun Seo, Jin Miyawaki, Isao Mochida, Seong-Ho Yoon, *Electrochim. Acta* 93 (2013) 236–240.
- [2] A.N. Morozovska, E.A. Eliseev, N. Balke, S.V. Kalinin, *J. Appl. Phys.* 108 (2013) 053712.
- [3] M. Nonnenmacher, M.P. O'Boyle, H.K. Wickramasinghe, *Appl. Phys. Lett.* 58 (1991) 2921.
- [4] Shrikant C. Nagpure, Bharat Bhushan, S.S. Babu, *J. Power Sources* 196 (2011) 1508–1512.
- [5] Jing Zhu, Kaiyang Zeng, Li Lu, *J. Appl. Phys.* 111 (2012) 063723.
- [6] Wilhelm Melitz, Jian Shen, Andrew C. Kummel, Sangyeob Lee, *Surf. Sci. Reports* 66 (2011) 1–27.
- [7] Vishal Panchal, Ruth Pearce, Rositza Yakimova, Alexander Tzalenchuk, Olga Kazakova, *Sci. Reports* 3 (2013) 2597.
- [8] Shigeki Kawai, Thilo Glatzel, Hans-Josef Hug, Ernst Meyer, *Nanotechnology* 21 (2010) 245704.
- [9] Hiroyuki Kawano, *Prog. Surf. Sci.* 83 (2008) 1–165.
- [10] Hendrik Bluhm, Takahito Inoue, Miquel Salmeron, *Surf. Sci.* 462 (2000) L599–L602.
- [11] Gang Ning, Bala Haran, Branko N. Popov, *J. Power Sources* 117 (2003) 160–169.
- [12] Hong-Li Zhang, Feng Li, Chang Liu, Jun Tan, Hui-Ming Cheng, *J. Phys. Chem. B* 109 (2005) 22205–22211.
- [13] Mengyun Nie, Dinesh Chalasani, Daniel P. Abraham, Yanjing Chen, Arijit Bose, Brett L. Lucht, *J. Phys. Chem. C* 117 (2013) 1257–1267.
- [14] U. Zaghloul, B. Bhushan, P. Pons, G. J. Papaioannou, F. Coccetti, R. Plana, *Nanotechnology* 22 (2011) 035705.
- [15] W.N. Hansen, G.L. Hansen, *Surf. Sci.* 481 (2001) 172–184.
- [16] S. Ono, M. Takeuchi, T. Takahashi, *Appl. Phys. Lett.* 78 (2001) 8.
- [17] M.D.V. Przychowski, G.K.L. Marx, G.H. Fecher, *Surf. Sci.* 549 (2004) 37–51.
- [18] A.N. Obraztsov, A.P. Volkov, A.I. Boronin, S.V. Kosheev, *Diam. Relat. Mater.* 11 (2002) 813–818.
- [19] A.S. Baturin, K.N. Nikolski, A.I. Knyazev, R.G. Tchesov, E.P. Sheshin, *Tech. Phys.* 49 (3) (2004) 342–344 [Translated from *Zhurnal Tekhnicheskoi Fiziki* 74, 3 (2004) 62–64].
- [20] Hyunbok Lee, Soohyung Park, Jiehyun Lee, Younjoo Lee, Dongguen Shin, Kwangho Jeong, Yeonjin Yi, *Appl. Phys. Lett.* 102 (2013) 033302.

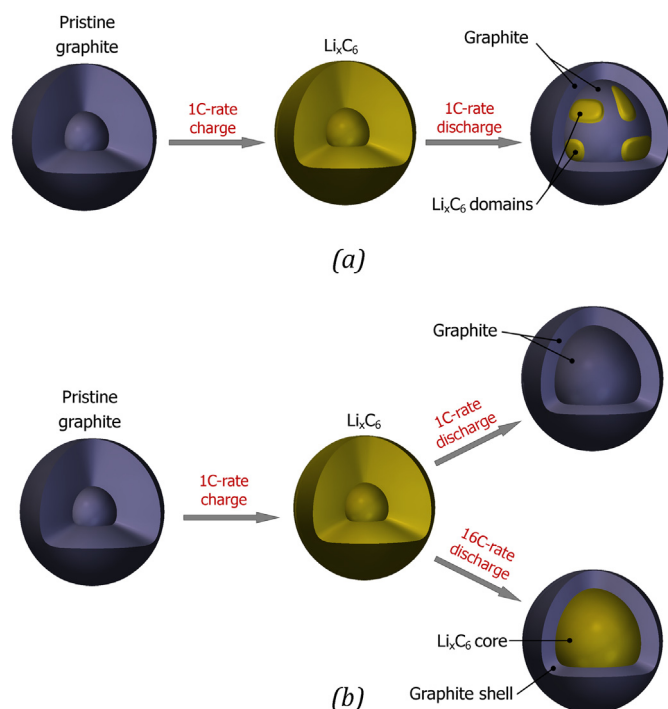


Fig. 8. Schematic illustration of (a) a “mosaic” and (b) a “radial” models of Li blocking within the bulk.

- [21] Kai Xie, Lian Duan, Deqiang Zhang, Juan Qiao, Guifang Dong, Liduo Wang, Yong Qiu, *J. Phys. D: Appl. Phys.* 43 (25) (2010) 252001.
- [22] S. Mizuno, H. Tochiwara, T. Kadowaki, H. Minagawa, K. Hayakawa, I. Toyoshima, *Surf. Sci.* 264 (1–2) (1992) 103–113.
- [23] S.S. Zhang, K. Xu, T.R. Jow, *Electrochim. Acta.* 48 (2002) 241–246.
- [24] Masaki Yoshio, Ralph J. Brodd, Akiya Kozawa, *Lithium-ion Batteries: Science and Technologies*, Springer, New York, USA, 2009.
- [25] Atsushi Funabiki, Minoru Inaba, Takeshi Abe, Zempachi Ogumi, *Carbon* 37 (1999) 1591–1598.
- [26] J.S. Gnanaraj, M.D. Levi, E. Levi, G. Salitra, D. Aurbach, John E. Fischer, Agnes Claye, *J. Electrochem. Soc.* 148 (6) (2001) A525–A536.
- [27] A.H. Whitehead, K. Edström, N. Rao, J.R. Owen, *J. Power Sources* 63 (1996) 41–45.
- [28] Yue Qia, Haibo Guo, Louis G. Hector Jr., Adam Timmon, *J. Electrochem. Soc.* 157 (5) (2010) A558–A566.
- [29] Vijay A. Sethuraman, Laurence J. Hardwick, Venkat Srinivasan, Robert Kostecki, *J. Power Sources* 195 (11) (2010) 3655–3660.
- [30] A.S. Andersson, J.O. Thomas, *J. Power Sources* 97–98 (2001) 498–502.